Supplementary Information

Multipolar Radiation of Quantum Emitters with Nanowire Optical Antennas

Alberto G. Curto[1], Tim H. Taminiau[1], Giorgio Volpe[1], Mark P. Kreuzer[1], Romain Quidant[1,2], Niek F. van Hulst[1,2]*

[1] *ICFO - Institut de Ciencies Fotoniques, Mediterranean Technology Park, 08860 Castelldefels (Barcelona), Spain*

[2] *ICREA - Institució Catalana de Recerca i Estudis Avançats, Barcelona, Spain*

*Corresponding author: Niek.vanHulst@ICFO.eu

Contents:

Supplementary Figures

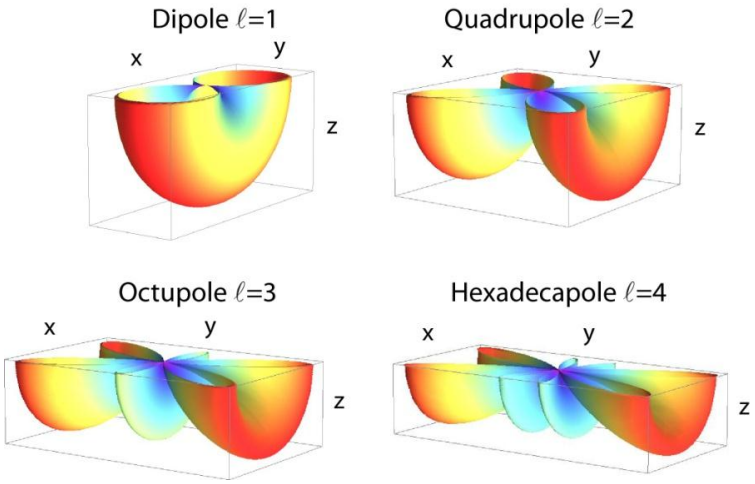

Supplementary Figure S1 | Angular radiation patterns of longitudinal multipoles in free space. Far-field emission of point longitudinal multipoles oriented along y in a homogeneous medium. In order to show a cross-section of the angular pattern, only the lower half space is displayed. In free space, the radiation patterns of longitudinal multipoles are axially symmetric with respect to the multipole orientation. On a glass substrate, however, the lobes that were axially symmetric in free space are projected into the substrate breaking the rotational symmetry.

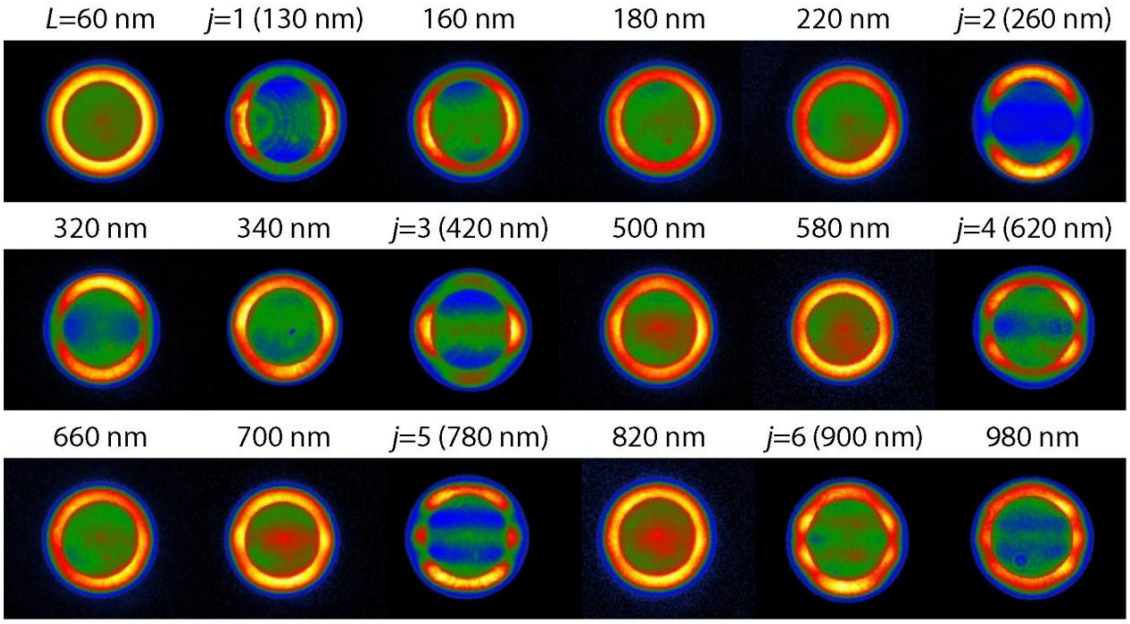

Supplementary Figure S2 | Evolution of angular patterns for antennas on and off resonance. Experimental angular radiation patterns for antennas of increasing length measured at the back focal plane of the microscope objective (colormap as in Figure 3). The coupling of the quantum dot to the antenna evolves on and off resonance for increasing lengths. This has an effect on the angular radiation pattern of the quantum-dot–antenna system. At resonance, the mode of the antenna determines the radiation pattern of the quantum dot. Off resonance, the pattern resembles the rotationally symmetric emission of a reference quantum dot on glass or on a small metal square (upper left corner). Some representative intermediate lengths are shown, not equally spaced.

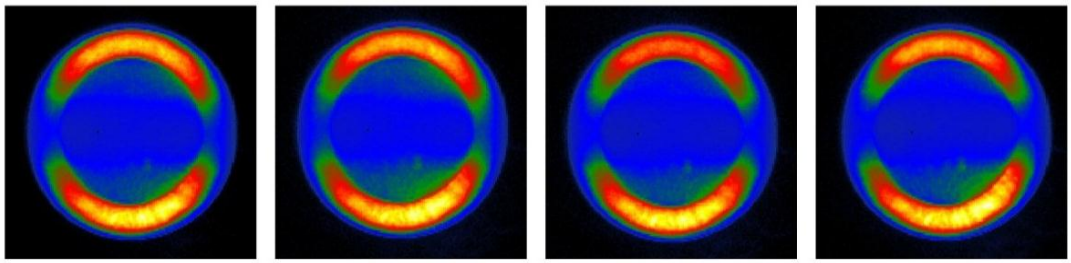

Supplementary Figure S3 | Repeatability of angular patterns for quadrupolar antennas. Experimental angular radiation patterns of four individual quadrupolar antennas with identical nominal antenna parameters, showing repeatable quadrupolar radiation as an example of the repeatability of the coupling of dipolar emitters to multipolar radiation allowed by our nanoscale positioning fabrication technique.

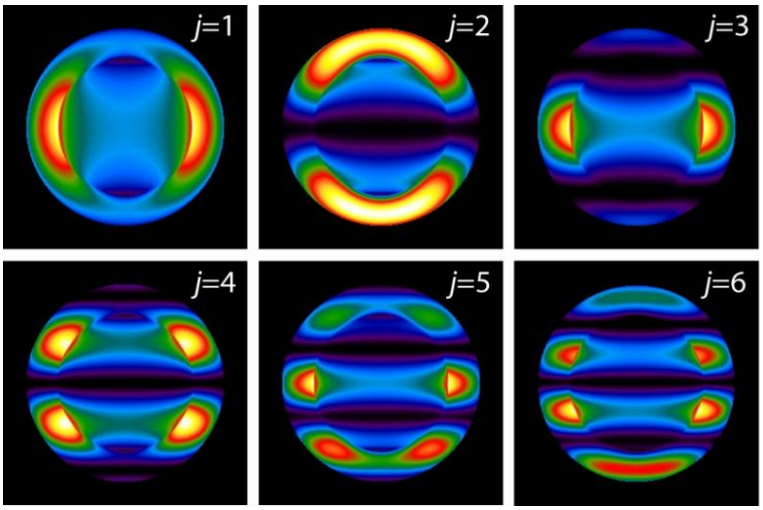

Supplementary Figure S4 | Angular radiation patterns of the pure antenna modes calculated using the one-dimensional model. The calculations of angular patterns in Fourier space use the antenna parameters retrieved by fitting the experimental angular patterns in Figure 3. The slight asymmetry in higher order modes is due to propagation losses of the surface plasmon in the nanowire.

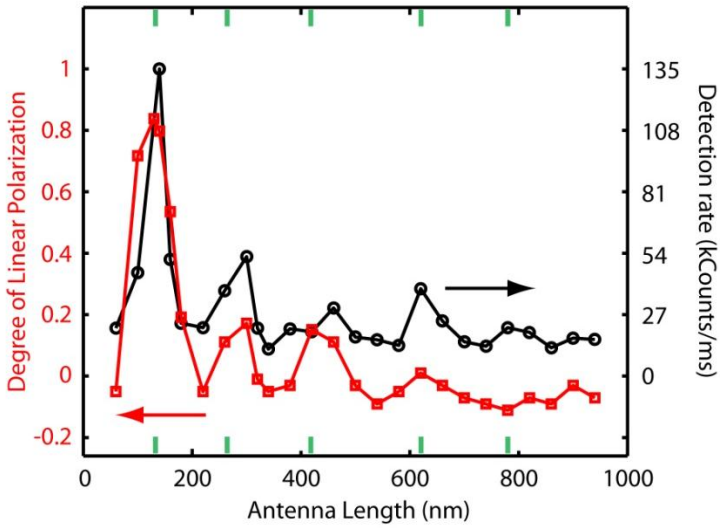

Supplementary Figure S5 | Comparison of detected counts per antenna and polarization for different nanowire lengths. Higher order resonant antennas radiate a comparable amount of photons to the dipole antenna. For example, the second resonance antenna radiates 40% as much as the first resonance. Interestingly, the oscillations in intensity follow those of the polarization, confirming the identification of resonant lengths. On the right axis, the counts per antenna were averaged over all antennas of identical length in an array, at an excitation power density of 1.08 kW/cm2. On the left axis, the degree of linear polarization is represented by the maximum of antenna array histograms (statistical mode). The resonant lengths identified in the radiation patterns of Figure 3 are highlighted with green vertical lines.

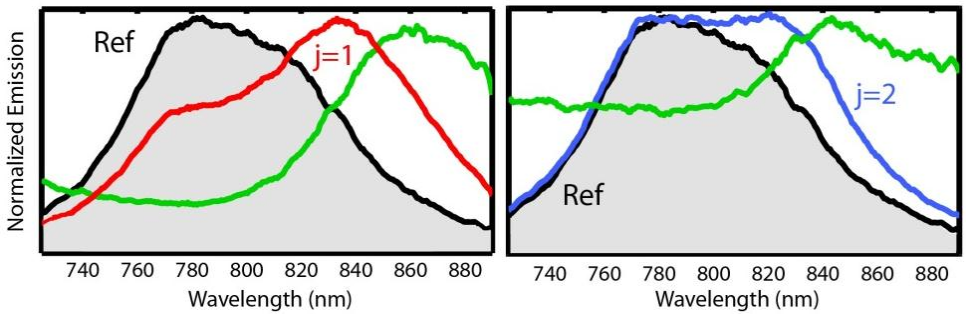

Supplementary Figure S6 | The emission spectrum is modified by coupling to the antenna. Due to the coupling of two oscillators (quantum dot and antenna), a spectral shift or modification is be expected in the emission of our hybrid systems [53, 54]. These shifts are most evident when the antenna is slightly detuned with respect to the natural quantum dot wavelength. The modified emission spectra are shown for quantum dots coupled to antennas, with the first (red line, left) and second (blue line, right) resonant modes detuned to the red of the QD emission. The average spectrum of such quantum dots on a non-resonant metal structure of 60 nm (Ref, black line) is very similar to the isolated quantum dot spectrum. A spectral enhancement is calculated (in green, antenna divided by reference) revealing the spectrum of emission enhancement of the antenna.This modification is evidence of the hybrid, coupled character of our sources. It also shows a lower coupling efficiency to the second order mode (weaker modulation of emission spectrum).

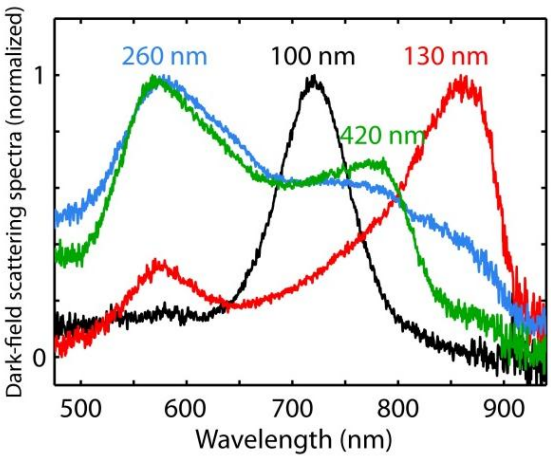

Supplementary Figure S7 | Dark-field scattering spectra of antennas of different lengths. Spectra were acquired with far-field unpolarized illumination under normal incidence. Under this configuration, excitation from the far field does not allow access to the quadrupolar mode (*L*=260 nm).

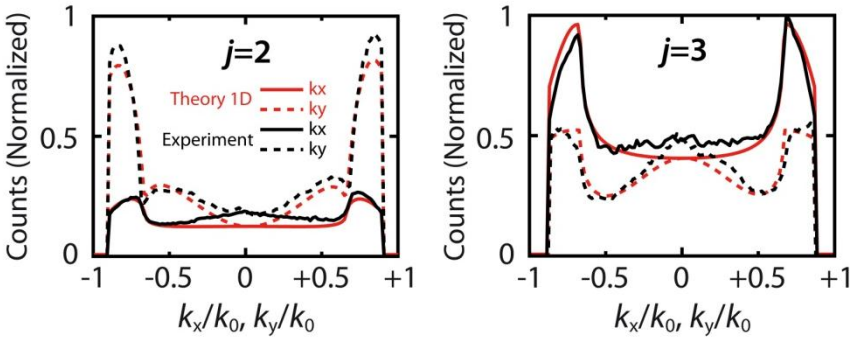

Supplementary Figure S8 | Cross sections of experimental angular radiation patterns and fitting with the one-dimensional resonator model for the first two multipolar modes. A radius of four pixels below the numerical aperture is removed from the experimental data because the collection efficiency of the objective starts decaying before reaching the nominal numerical aperture. The 1D model and the experimental results are in good agreement.

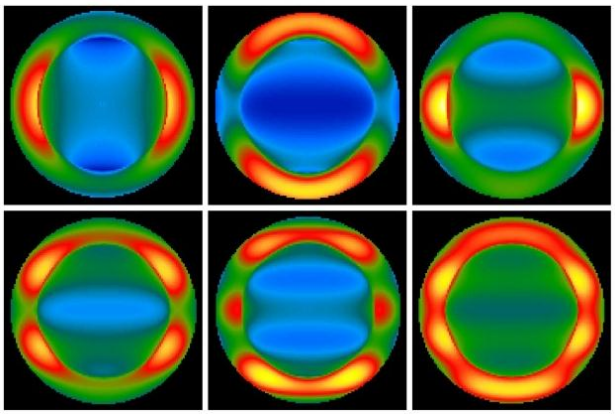

Supplementary Figure S9 | Results of fitting the experimental angular radiation patterns with a multipolar expansion.

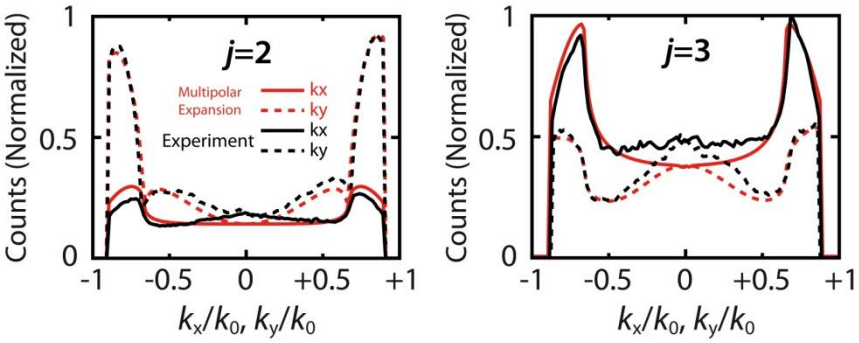

Supplementary Figure S10 | Cross sections of experimental angular radiation patterns and fitting with a multipolar expansion for the first two multipolar modes. A radius of four pixels below the numerical aperture was removed from the experimental data because the collection efficiency of the objective starts decaying before reaching the nominal numerical aperture. The multipolar expansion and the experimental results are in good agreement.

Supplementary Tables

λ_{SP} (nm)	k_i/k_0	$\phi\,\lambda_{SP}/2\pi$ (nm)	$\lvert r\rvert$
313±3	0.150±0.025	34±2	0.7±0.03

Supplementary Table S1 | Antenna parameters retrieved from fitting to the experimental average polarization with the 1D resonator model. Results of fitting to the average of all measured antennas (blue line in Figure 2b).These results are inhomogeneously broadened due to a distribution of imperfections in the wires (polycrystalline structure) and accuracy in quantum dot positioning and orientation. As a result, the parameters of the antenna that describe the losses of the resonator (k_i and $|r|$) are mostly determined by inhomogeneous broadening (k_i is effectively increased by the broadening, $|r|$ is decreased). On the other hand, the parameters that determine the position of the resonances (λ_{SP} and ϕ) do give an accurate estimate of the average properties of the antennas and allow us to determine the resonant antenna lengths.

j (mode)	λ_{SP} (nm)	k_i/k_0	$\phi\,\lambda_{SP}/2\pi$ (nm)	$\lvert r\rvert$	R^2 (fit quality)
1	280±10	0.01±0.03	32±2	1±0.05	0.980
2	250±10	0.04±0.03	32±2	1±0.05	0.987
3	280±10	0.04±0.03	32±2	1±0.05	0.982
4	330±10	0.01±0.03	32±2	1±0.05	0.967
5	330±10	0.08±0.02	32±2	1±0.05	0.976
6	310±10	0.08±0.02	32±2	1±0.05	0.971

Supplementary Table S2 | Antenna parameters and quality of the fit of the experimental angular patterns with the 1D resonator model. The values of the retrieved antenna parameters denote the lower losses (k_i and $|r|$) and the higher coupling efficiency of the antennas (green squares in Figure 2b) when compared to the results of the polarization fit to the average antenna (blue line in Figure 2b and Supplementary Table S1). The uncertainties in the antenna parameters are given by the spacing between consecutive steps in the exploration of antenna parameter space.

j (mode)	*RMSE* (average error)
1	0.0052
2	0.0039
3	0.0073
4	0.0088
5	0.0074
6	0.0105

Supplementary Table S3 | Quality of the results of fitting the experimental angular patterns with a multipolar expansion. The root-mean-square error (RMSE, square root of the square of the residuals averaged over all pixels within the numerical aperture) is small compared with the maximum value of normalized counts in the back focal plane (unity)

Supplementary Notes

Supplementary Note 1: Theoretical description as a one-dimensional cavity:

The theoretical calculations of Figures 2 and 3 are based on a previously published model for the interaction of nanowire antennas with quantum emitters and radiation [24]. We describe the antenna as a one-dimensional (1D) cavity for surface plasmons. The origin is chosen at the centre of the antenna and the antenna axis is oriented along *y*. Plasmons travel along the antenna (length *L*) with complex wave vector *k* and are reflected at the antenna ends with complex reflection coefficient $r = |r|e^{i\phi}$. The plasmon propagating along the antenna has a wavelength λ_{SP} ($Re(k)=2\pi/\lambda_{SP}$) and losses determined by $Im(k)=k_i$.

For an electric dipole at one of the ends of the antenna (position $y=-L/2$), the current distribution along the antenna is given by:

$$I(y) \propto \frac{e^{\frac{ikL}{2}}(r+1)}{1-r^2e^{2ikL}}\left(e^{iky} - re^{ikL}e^{-iky}\right) \tag{S1}$$

From this current distribution we obtain the emitted field as:

$$\mathbf{E}(k_x, k_y) = \mathbf{E_0}(k_x, k_y)\int_{-L/2}^{L/2} I(y)e^{-ik_y y}\,dy \tag{S2}$$

in which k_x and k_y are the projections of the wave vector (magnitude k_0) of the emitted radiation along *x* and *y*, and $\boldsymbol{E}_0(k_x, k_y)$ is the electric field emitted by a *y*-oriented electric dipole above an air-glass interface. This dipole is situated 15 nm away from the interface on the air side, at half the antenna height of 30 nm in the experiment. Solutions for $\boldsymbol{E}_0$ can be found for example in chapter 9 of Novotny and Hecht [50]. In contrast to our previous work [24], *r* is set as a constant independent of *L*. The small differences in the emission patterns caused by this choice are within the experimental errors.

Equation (2) directly yields the back focal plane image for the antenna mode:

$$P^{1D\ model}(\mathrm{k_x}, \mathrm{k_y}) = \frac{|\mathbf{E}(\mathrm{k_x}, \mathrm{k_y})|^2}{2\eta} \tag{S3}$$

in which η is the impedance of the medium.

The angular patterns for these pure antenna modes are shown in Supplementary Figure S4 using the antenna parameters retrieved from the experiment in Figure 3.

For the polarization analysis, the emitted field is propagated through a confocal imaging system using the angular spectrum representation [51, 52]. The dependence predicted by this theory for measurements in our optical system is shown in Figure 1c.

1.1 Fitting of average polarization with 1D model:

We can model the experimentally obtained polarization versus length by using the 1D model presented above, adding two contributions in *x* and *y* polarizations to account for emission that was not coupled to the antenna mode and was thus not present in the pure antenna model. With the addition of two independent contributions in perpendicular polarizations, we account for the existence of weak transversal modes and partially polarized gold auto-luminescence, which further contribute to depolarization of the pure antenna signal. With this, the average of the

degree of linear polarization, taken experimentally over approximately 200 antennas per length, can be described by:

$$DOLP^{Exp}(L) = \frac{I_x^{1D\ model}(L,\lambda_{SP},k_i,r,\phi) - I_y^{1D\ model}(L,\lambda_{SP},k_i,r,\phi) + \alpha\, I_x^{uncoupled} - \beta\, I_y^{uncoupled}}{I_x^{1D\ model}(L,\lambda_{SP},k_i,r,\phi) + I_y^{1D\ model}(L,\lambda_{SP},k_i,r,\phi) + \alpha\, I_x^{uncoupled} + \beta\, I_y^{uncoupled}} \quad (S4)$$

where I_x and I_y are counts that would be detected through a linear polarizer along x or y, respectively.

A nonlinear fit to the experimental average degree of polarization yields the relative weights of the antenna mode and the two background polarizations (α,β). By repeating this fit for different sets of antenna parameters ($\lambda_{SP}, k_i, r, \phi$), we find an optimum set of parameters that describes more accurately the average polarization. The results of fitting to the average of all measured antennas (blue line in Figure 2b) yield the parameters contained in Supplementary Table S1.

1.2 Fitting of individual angular patterns with 1D model:

The radiation pattern (back focal plane image, $P^{Exp}(k_x, k_y)$) of each individual antenna was reproduced using a least-squares linear fit to find the optimal weights (*A* and *B*) of the antenna mode ($P^{1D\ model}$, shown in Supplementary Figure S4) and the uncoupled background ($P^{dipole\ x}$ and $P^{dipole\ y}$):

$$P^{Exp}(k_x, k_y) = A \cdot P^{1D\ model}(k_x, k_y) + B \cdot \left(P^{dipole\ x}(k_x, k_y) + P^{dipole\ y}(k_x, k_y)\right) \quad (S5)$$

In order to make the computational burden of solving this fitting problem manageable, the angular patterns for different sets of parameters were calculated only once so that only the weights *A* and *B* had to be found, while the antenna parameters were varied in a systematic way to explore the parameter space. By repeating this linear fit for different sets of antenna parameters, we found the best fit to the individual antennas shown in Figures 3i-n with retrieved antenna parameters and quality of the fit shown in Supplementary Table S2. Two cross sections are also shown in Supplementary Figure S8.

We fit the data throughout the manuscript to a superposition of an emission pattern characteristic of the antenna and a rotationally symmetric unpolarized background emission that does not carry the antenna characteristics (uncoupled emission). This incoherent background is an approximation, which fits all experimental results. Several arguments support this approach. First, part of the uncoupled background is luminescence of the antenna itself and is incoherent with any quantum dot luminescence. Second, our quantum dots have a broad emission spectrum and a largely unpolarized emission pattern due to its degeneracy in transition dipole moment, which ultimately have to be added together incoherently. Multiple quantum dots also introduce similar effects. We also note that it is possible that interference of coherent terms is small due to the differences in phase, polarization and angular pattern of the QD dipole transitions and the antenna emission. All these mechanisms contribute to average out the visibility of the potential interference and we can treat, as a reasonably simplified approximation for our experiment, the luminescence that is not coupled to the antenna as incoherent. Our fitting results are indeed in agreement with the experimental data under such an approximation.

Supplementary References

50 Novotny, L. & Hecht, B. Principles of Nano-Optics. (Cambridge University Press, 2006).

51 Wolf, E. Electromagnetic diffraction in optical systems. I. An integral representation of the image field. *Proc. Roy. Soc. London A* **253**, 349-357 (1959).

52 Richards, B. & Wolf, E. Electromagnetic diffraction in optical systems II. Structure of the image field in an aplanatic system. *Proc. Roy. Soc. London A* **253**, 358-379 (1959).

53 Ringler, M. et al. Shaping Emission Spectra of Fluorescent Molecules with Single Plasmonic Nanoresonators. *Phys. Rev. Lett.* **100**, 203002 (2008).

54 Biteens, J. S. et al. Spectral tuning of plasmon-enhanced silicon quantum dot luminescence. *Appl. Phys. Lett.* **88**, 131109 (2006).